## W&M ScholarWorks

12-2021

# Hyperspectral Infrared Imaging of Surface Phonon-polaritons in SrTiO3

D. J. Lahneman

M. M. Qazilbash

# Hyperspectral infrared imaging of surface phonon-polaritons in SrTiO₃

D. J. Lahneman ● and M. M. Qazilbash*

*Department of Physics, College of William & Mary, Williamsburg, Virginia 23187-8795, USA*

Polaritons have a demonstrated impact on nanophotonic applications in the midinfrared through visible spectral range. Surface phonon-polaritons (SPhPs) offer a way to bring the potential of polaritons to the longer infrared wavelengths. Strontium titanate (STO) is a perovskite polar dielectric with diverse technologically advantageous properties and it can support SPhPs in a uniquely broad spectral range of the far infrared. Despite these advantages, STO has mostly been overlooked as a nanophotonic material. In this work we investigate SPhP propagation in STO in the far-infrared through midinfrared spectral range using broadband, near-field nanospectroscopy. We developed a tabletop, laser sustained plasma light source that enabled us to obtain amplitude and phase resolved hyperspectral line scan maps of SPhPs across the surface of the STO sample. Analytical modeling of experimental data reveals the dispersion characteristics of SPhPs in STO. This work establishes STO as a platform for perovskite-based broadband far-infrared and terahertz nanophotonics.

## I. INTRODUCTION

Polaritons are quasiparticles formed from the strong coupling of photons with charge excitations in materials such as plasmons, phonons, and excitons [1–4]. Polaritons have already made significant impact in many areas of research including efforts toward room temperature Bose-Einstein condensation [4,5], superfluidity and quantized vortices [6,7], room temperature polariton lasers [8,9], all-optical transistors [10], and efficient energy conversion [11]. Plasmon- and exciton-polaritons have demonstrated utility from the midinfrared through the visible range. However, as the wavelengths get further into the less explored far-infrared and terahertz spectral range, limitations occur due to lack of available sources and detectors. It is in this spectral range that surface phonon-polaritons (SPhPs) show great potential to carry over the technological advantages of polaritons. SPhPs are surface electromagnetic waves that result from the coupling of photons with optical phonons in dielectrics. In contrast, surface plasmon-polaritons (SPPs) are surface electromagnetic waves that arise from the coupling of photons to free electrons in metals. SPhPs arise in a range of frequencies dictated by the optical phonons of the dielectric, which often occur below $1000$ cm$^{-1}$ frequency. SPhPs already have been proven in applications such as coherent thermal emission [12], enhanced light-matter interactions [13], high-density infrared data storage [14], metamaterials [15–17], terahertz wave generation [18], and electrically pumped SPhP-based lasers [19].

The far-infrared SPhP spectrum has recently been experimentally resolved in strontium titanate (STO) [20–23]. STO is a highly stable material. It is a polar dielectric that exhibits a diverse range of electronic and optical properties that make it an exciting technological material. STO is transparent to visible light with a band gap of ∼3.2 eV while having excellent paraelectric, dielectric, and optoelectronic properties [24–26]. Upon doping with electrons, either through niobium or iron doping or via oxygen vacancies, STO can transition to a very stable metallic state [27–34]. Furthermore, STO can support exotic states such as superconductivity and a two-dimensional electron gas [35–38]. As a cubic perovskite, STO is a common substrate for lattice matching or to provide strain to a number of functional oxide films [39]. Many advancements have been made in obtaining low-impurity and high crystalline quality bulk samples of STO as well as treatments to produce high-quality surfaces. However, very little work has been done toward realizing the potential of STO as an infrared nanophotonic platform. Only recently has STO been put in perspective as a unique polar dielectric in the infrared due to its ability to support both a midinfrared SPhP and a far-infrared SPhP [21,40]. Most work discussing STO has been constrained to the midinfrared, only covering the higher-frequency SPhP without probing wavelengths longer than a free space wavelength of ∼20 μm [22,23,41].

For both SPPs and SPhPs, the conditions for a propagating surface wave are that the real part ($\varepsilon_1$) of the dielectric function is negative while the imaginary part ($\varepsilon_2$) is small. For SPhPs in polar dielectrics, these conditions are met between the transverse optical (TO) and longitudinal optical (LO) phonons, called the reststrahlen band [42]. Figure 1(a) displays the reflectance of STO showing two reststrahlen bands. The midinfrared (mid-IR) band manifests between the TO and LO phonon modes primarily related to motion of the lighter oxygen atoms, while the far-infrared (far-IR) band results from a combined contribution of the TO and LO phonon modes primarily related to motion of the heavier strontium and titanium atoms [43]. Figure 1(b) shows the real and imaginary parts of the complex dielectric function revealing that the reststrahlen bands occur when $\varepsilon_1$ is negative. It is interesting to note that the low-frequency, very strong TO strontium
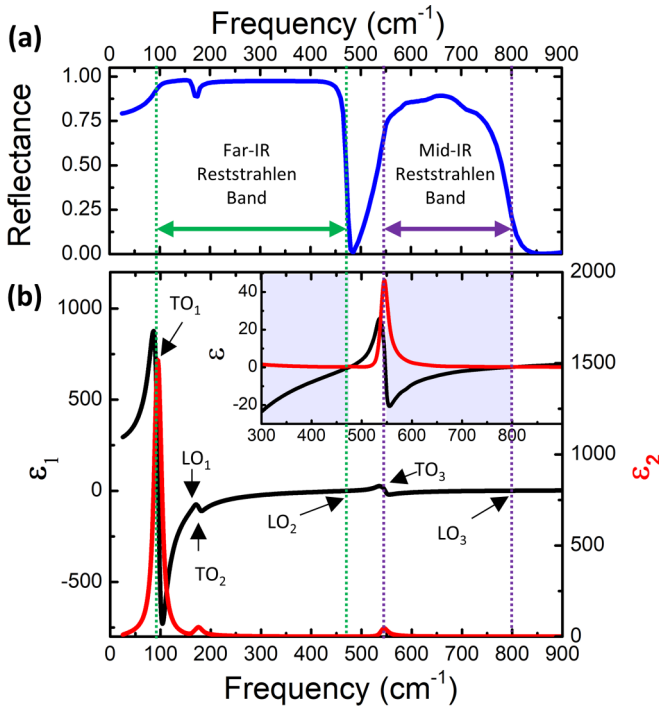
*mmqazilbash@wm.edu

**(a)**



FIG. 1. (a) Reflectance of STO demonstrating the two reststrahlen bands. (b) Real ($\varepsilon_1$) and imaginary ($\varepsilon_2$) parts of the dielectric function with the optical phonon modes indicated by vertical dashed lines. The inset shows the zoomed-in view of the frequency-dependent real (black) and imaginary (red) parts of the dielectric function. The shaded region shows the negative $\varepsilon_1$ regions. The optical constants for STO were taken from Ref. [46].

related mode located at $\sim 87$ cm$^{-1}$ takes $\varepsilon_1$ negative for a significant portion of the far-infrared spectrum. It is STO's ability to support SPhP modes across this large spectral range that make it a good candidate for far-infrared nanophotonic applications. While many polar dielectric materials, including $\alpha$-MoO$_3$, Al$_2$O$_3$, $\beta$-Ga$_2$O$_3$, and GaAs support SPhP modes in more narrow regions of the mid- and far infrared, few materials support them over such a wide far-infrared and terahertz spectral range as STO [40,44,45]. It is this broadband window for SPhPs in the far infrared combined with STO supporting two separate SPhP branches across the mid- and far infrared that make the case for STO as a far-infrared nanophotonic platform. Through the application of established techniques such as nanopatterning of geometric structures on the surface, SPhPs in STO should be tunable over a large window of the far infrared. For example, it has been shown that localized SPhPs can be tuned across the reststrahlen band by nanopatterning pillars of varying radius on SiC [15]. Applied to STO, these methods should allow selective and tunable optical response over the large bandwidth of the far infrared inside of STO's lower reststrahlen band, paving the way for frequency tailored far-infrared and terahertz sensors, metamaterials, and coherent far-infrared and terahertz sources.

There exists a mismatch in the momentum needed to excite a SPhP with a freely propagating photon. Scattering-type scanning near-field optical microscopy (sSNOM) has been proven to be a particularly useful method to directly excite

and probe SPhPs [47]. In this method, infrared radiation is focused to a metal-coated atomic force microscope (AFM) tip which induces strong near fields at the tip apex. These strong near fields interact with the sample underneath and this interaction is encoded in the scattered far-field radiation. The AFM tip is operated in tapping mode to extract the near-field interaction from the background contributions [48]. This technique allows nanometer-scale optical properties to be studied at a spatial resolution limited only by the radius of the AFM tip apex [49–53]. Due to this high-field confinement, the tip can provide the necessary momentum to excite SPhPs in dielectric materials [54]. This overcomes the wave vector (momentum) mismatch between the incident light, $k = (\omega/c)$, and the real part of the SPhP wave vector [Re($k_p$) = $2\pi/\lambda_p$]. The complex-valued SPhP wave vector is given by

$$k_p = \text{Re}(k_p) + i\text{Im}(k_p) = \left(\frac{\omega}{c}\right)\sqrt{\frac{\varepsilon_m \varepsilon_a}{\varepsilon_m + \varepsilon_a}}. \quad (1)$$

Here $\omega$ is the angular frequency of incident light, $c$ is the speed of light, $\varepsilon_m$ is the complex dielectric function of the medium supporting SPhPs, and $\varepsilon_a$ is the complex dielectric function of the ambient medium [42]. Work has been done using sSNOM in the midinfrared spectral range to characterize polar dielectric materials such as SiC and low-dimensional van der Waals materials, e.g., hexagonal boron nitride. sSNOM has been utilized to excite, launch, and observe interference of these SPhPs by either single line laser or broadband techniques [55–64]. Most of the work to characterize and realize applications for these SPhPs has been in the midinfrared ($>700$ cm$^{-1}$) where there are detectors and sources compatible with sSNOM. For lower SPhP frequencies ($<700$ cm$^{-1}$), options are generally limited to either a synchrotron beamline or free electron laser [65–69].

In this paper, we explore the propagation and interference of the SPhPs on STO by coupling a recently developed, tabletop laser sustained plasma light source (LSPLS) to our sSNOM set up. This integrated light source allows ultrabroadband infrared nanospectroscopy (nano-FTIR) to be accessed in a tabletop experiment down to frequencies as low as 400 cm$^{-1}$, limited by the detector cutoff. This allows direct access to excite and probe SPhPs with sSNOM in the broad far-infrared reststrahlen band in STO. First, we introduce this LSPLS, then we demonstrate its ability to probe SPhP resonances in SiO$_2$, a material whose SPhP resonances are already well characterized with sSNOM. Then we use the LSPLS and sSNOM to resolve and map propagating SPhPs on STO launched by a gold (Au) edge. Through analytical modeling of the experimental data, we obtain the dispersion of two SPhP branches.

## II. EXPERIMENTAL METHOD

We developed in house a tabletop laser sustained plasma light source to provide the necessary high-intensity broadband radiation for nano-FTIR. The LSPLS is a direct upgrade to our previously developed argon plasma light source (APLS) [20,21,70]. A schematic diagram of the experimental setup of the LSPLS and sSNOM can be seen in Fig. 2(a). The LSPLS is described in the Appendix. We performed sSNOM measurements on STO and SiO$_2$ samples using a commercial
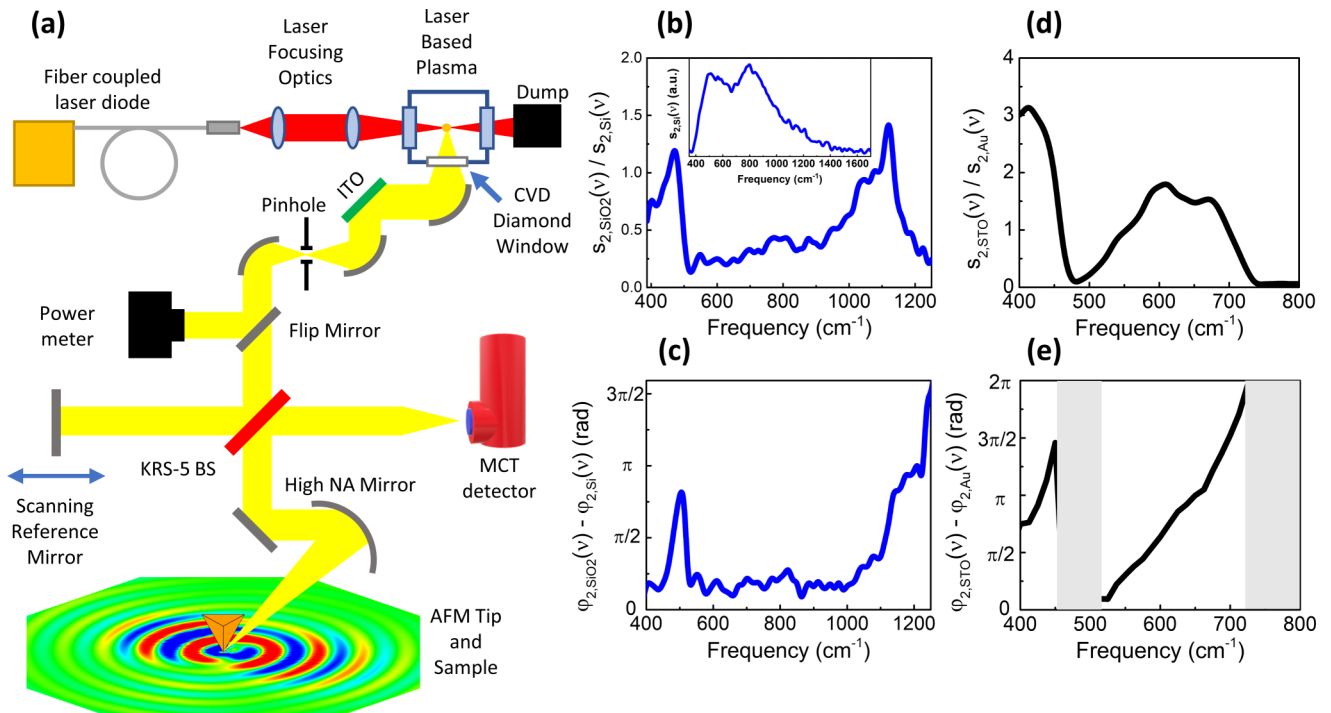
FIG. 2. (a) Schematic of the beam path used in our LSPLS system with the red representing the near-infrared laser used to sustain the plasma and the yellow representing the broadband radiation from the plasma. Broadband nano-FTIR point spectra obtained with the LSPLS setup on 100 nm $SiO_2$ on Si showing $n = 2$ amplitude (b) and phase (c) referenced to Si. The reference spectrum on Si is shown in the inset of (b). The $n = 2$ amplitude (d) and phase (e) point spectra of bulk STO referenced to an Au film deposited on part of the STO. The spectra on STO were obtained far ($> 500$ $\mu$m) from the Au film. The phase is indeterminate in the spectral regions depicted by the gray areas in (e) because the scattering amplitude from STO is negligibly small in these spectral regions.

microscope from Neaspec GmbH. Infrared light is focused onto the apex of a metal-coated AFM tip. The sSNOM obtains sample information encoded in the scattered light from the tip-sample system. The AFM tip localizes the light to a lateral resolution limited only by the radius of the tip apex [48]. Broadband near-field spectra can be acquired with the sSNOM instrument and the spectra reveal the broadband, frequency-dependent infrared behavior of the sample at nanometer scale spatial resolution. This method allows us to obtain infrared properties by circumventing the Abbe diffraction limit. It also enables enhanced surface sensitivity when compared to the larger penetration depths of conventional far-field Fourier transform infrared (FTIR) methods [71–73]. As can be seen in Fig. 2(a), we take broadband nanospectroscopy data by coupling the laser sustained plasma light source to the sSNOM system. The sSNOM optical setup [Fig. 2(a)] is similar to that described in our previous works [20,21]. The broadband infrared radiation from the plasma is collected and collimated by an off-axis parabolic (OAP) mirror with a 2 in. focal length. It is reflected at a 45° angle of incidence off an indium tin oxide (ITO) coated glass mirror. This mirror transmits the unwanted near-infrared and visible radiation and reflects the mid- and far-infrared radiation from the plasma. The reflected beam is then focused through a 200 $\mu$m pinhole by an OAP with a 4 in. focal length to improve the spatial coherence of the beam. The spatial coherence of the beam incident on the beam splitter is important for optimal interference between the tip-scattered radiation and the reference beam. After the pinhole, the beam is collimated using an OAP

mirror with a 1 in. focal length yielding a beam diameter of about 10 mm. A power of $\approx 1$ mW is measured in the beam after the 200 $\mu$m diameter pinhole in the spectral range between 400 and 5800 cm$^{-1}$ (excluding the spectral range between $\approx 1700$ and 2500 cm$^{-1}$ due to two-phonon absorption in the diamond window of the LSPLS). This beam is then incident on a KRS-5 beam splitter that transmits part of the beam toward the tip-sample system and reflects part of it toward the movable reference mirror. The transmitted beam is focused by a proprietary OAP onto the AFM tip. The AFM tip used in the experiment is supplied by Neaspec GmbH. The tip is coated with platinum-iridium and has a radius of curvature of $\sim 60$ nm. The scattered signal from the tip-sample system is then recollected with the same proprietary OAP and recombined with the beam reflected off the movable reference mirror and brought to a focus at a liquid nitrogen cooled Infrared Associates (FTIR-22-0.100) MCT photoconductive detector with an active area of $10^{-4}$ cm$^2$, a noise equivalent power of 0.84 pW Hz$^{-1/2}$, a spectral bandwidth of 400–5000 cm$^{-1}$, and a preamp with a 1 MHz bandwidth. The AFM tip is operated in tapping mode with an oscillation frequency of $\tilde{\nu} \approx 250$ kHz and a tapping amplitude of $\sim 80$ nm. To suppress the background, the signal recorded by the detector is demodulated at harmonics $n\tilde{\nu}$ of the tip oscillation frequency $\tilde{\nu}$, where the higher harmonics $n = 2, 3$ contain little to no background contamination. After demodulation, we obtain a scattered amplitude $s_n$ and a scattered phase $\phi_n$.

Initially an AFM topography image of the sample is obtained to map the STO and Au edge location. Note that the

STO sample has a 225 nm thick Au film deposited on part of the sample. The tip is brought into contact at the desired location on the sample and the movable reference mirror is scanned a set distance which generates an interferogram. A Fourier transform is applied to this interferogram to generate the near-field spectrum. To eliminate the instrumental features from the spectrum such as the detector responsivity, beam splitter, and LSPLS emission features, a normalization spectrum is obtained over a spectrally featureless material such as Au or Si. For point spectroscopy, the tip is kept in the same position on the sample and multiple interferograms are averaged to obtain a high signal to noise ratio spectrum. For a hyperspectral line scan, the tip moves along a set path with a spatial resolution of 1.5 $\mu$m collecting a full interferogram at each point of the line scan. A spectrum is obtained upon Fourier transform of an interferogram. The line scan process generates a two-dimensional hyperspectral image where the $x$ axis is the real space location of the tip and the $y$ axis is the frequency-dependent spectrum of the near-field amplitude or phase at that location. All the spectra in this paper, including the hyperspectral line scan, are taken with a spectral resolution of 12.5 cm$^{-1}$. The spectra obtained with the hyperspectral line scan are zero padded to improve image quality. The beam path and sSNOM system are enclosed in a dry and $CO_2$-free air purge to eliminate unwanted spectral features from water and $CO_2$.

## III. RESULTS AND DISCUSSION

First, a calibration sample was studied to observe known SPhP resonances in SiO$_2$. The sample studied consisted of an $\approx$ 100 nm layer of SiO$_2$ over silicon. We obtain an ultrabroadband near-field spectrum over the 400–1250 cm$^{-1}$ frequency ($\nu$) range which resolves two separate SPhP resonances that occur in SiO$_2$, seen in the amplitude and phase [Figs. 2(b) and 2(c), respectively]. The higher-lying resonance at 1130 cm$^{-1}$ has been characterized in many other near-field works [20,21,74,75] while the lower-lying resonance at 450 cm$^{-1}$ has only been observed by sSNOM utilizing an infrared synchrotron beamline [69]. Our observation of this lower-lying mode with our tabletop LSPLS system demonstrates the powerful utility of this source for far-infrared near-field nanospectroscopy. We then perform broadband near-field infrared experiments on single crystal STO. We obtain amplitude and phase spectra [Figs. 2(d) and 2(e)] on STO very far ($> 500$ $\mu$m) from the Au edge to characterize the near-field spectrum of STO. We see the two SPhP resonances that have been observed previously on bulk STO with the sharper low-frequency resonance occurring at $\approx$ 425 cm$^{-1}$ and the broader high-frequency resonance occurring at $\approx$ 675 cm$^{-1}$ [21]. The peaks occur inside the respective reststrahlen bands in STO [Fig. 1(a)], and arise from resonant near-field coupling between STO and the AFM probe geometry.

We then map the SPhPs in STO by obtaining an amplitude and phase resolved hyperspectral line scan in the vicinity of the Au edge. We orient the sample such that the Au edge is perpendicular to the in-plane projection of the tip illumination wave vector. Figure 3(a) shows a basic schematic of how the tip is scanned a distance away from the Au edge

while the broadband illumination, having a focused spot size diameter of $\sim$120 $\mu$m set by the pinhole, allows simultaneous tip illumination while launching SPhPs from the Au edge. Figures 3(b) and 3(c) show the amplitude and phase resolved near-field hyperspectral line scan showing the two SPhP resonances that occur in STO. As the tip is scanned away from the Au edge frequency-dependent interference fringes can be seen in both resonances. Taking single frequency cuts [Figs. 3(d) and 3(e)] of the hyperspectral line scan demonstrates clear fringes in both the amplitude and phase whose fringe spacing decreases with increasing illumination frequency. Another way to view this Au edge distance dependent SPhP interference is to look at the spectra as a function of distance. To increase the signal to noise ratio (SNR) from the hyperspectral line scan, point spectra were obtained by placing the tip at select distances from the Au edge in the same location and experimental geometry as the hyperspectral line scan. For these spectra, ten interferograms were collected and averaged to reduce the noise in the amplitude and phase, revealing clear peak shifts in the spectrum that result from the propagating SPhPs interfering with the incident tip illumination. These peak shifts match the hyperspectral line scan spectra at the same distance. Figures 3(f) and 3(g) show the amplitude and phase spectra obtained at select distances from the Au edge.

Our experimental geometry is similar to that used in previous works: SPhPs launched from a straight Au edge on SiC and a boron nitride slab [55,76,77], infrared plasmon-polaritons launched from a straight Au edge on graphene [78], and visible plasmon-polaritons on Au launched from a slit [79]. As already described by Huber *et al.*, the incident field at the tip is a superposition of the incident illumination $E_i$ at the tip position $x$, and the Au edge launched evanescent SPhP field at the tip position $E_p(x, z) = f_0 E_0 e^{i(k_{p,x}x + k_{p,z}z + \varphi_0)}$, where $E_0 = E_i e^{-ik\cos(\alpha)x}$ is the illumination field at the Au edge [55]. Here, $k_{p,x}$ and $k_{p,z}$ are the complex-valued SPhP wave vectors in the $x$ and $z$ direction and $\alpha$ is the angle between the sample surface and the direction of the incident light ($\alpha$ is set to be 30° by our instrument). We assume plane wave illumination with wave vector $k$. We account for the relative field amplitude $f_0 = |E_p(x = 0, z = 0)|/|E_i|$, and excitation phase $\varphi_0$, based on experimental data. We represent the scattered field from the tip as $E_s = \alpha_{\text{eff}}(z)[E_p + E_i]$, where $\alpha_{\text{eff}}(z)$ is the effective polarizability describing the near-field interaction between the tip and sample. Since the decay length of the surface polariton field is much larger than the tapping amplitude of the tip we can simplify the model by approximating $E_p(x, z) \approx E_p(x, 0)$. All together we can express the signal scattered from the tip at the $n$th harmonic of the tapping frequency to be

$$E_{s,n}(x) = \alpha_{\text{eff},n}[1 + f_0 e^{i\{[k_{p,x} - k\cos(\alpha)]x + \varphi_0\}}]E_i, \quad (2)$$

with $\alpha_{\text{eff},n}$ representing the $n$th harmonic of $\alpha_{\text{eff}}(z)$ which is constant when scanning over homogenous materials [48,80]. Using Eq. (2), the experimental fringe spacing at each frequency was fit [Figs. 4(a)–4(d)] to extract the complex-valued SPhP wave vector, $k_{p,x}$. The real part, Re($k_{p,x}$), depends on the fringe spacing, and its dispersion is plotted in Fig. 4(e). The data points of Re($k_{p,x}$), shown on the dispersion plot, lie close to the theoretical dispersion calculated from the generic SPhP theory [Eq. (1)] using published STO optical constants [Fig. 4(e)] [46]. Our geometry for mapping propagating
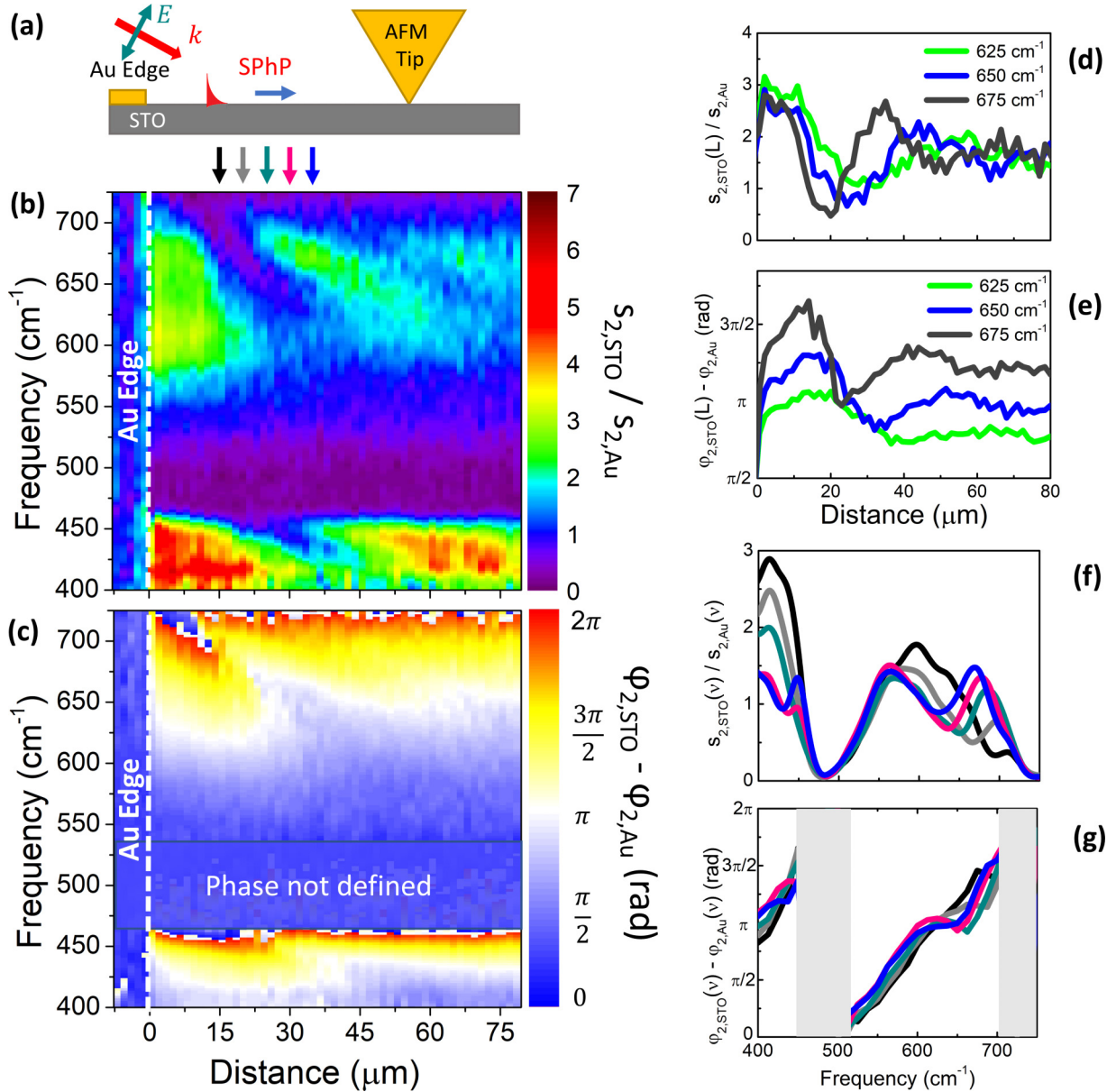
FIG. 3. (a) Schematic side view of the experiment showing the incident illumination and tip-sample system for studying the SPhPs on STO. The tip, starting over Au, is scanned away from the Au edge while the broadband $n = 2$ amplitude (b) and phase (c) spectra are measured. The spectra are normalized to an Au reference spectrum. Amplitude (d) and phase (e) line cuts at representative frequencies from (b,c), respectively, demonstrating frequency-dependent fringe spacings. The $n = 2$ amplitude (f) and phase (g) spectra at different distances from the Au edge [indicated by arrows in (b)] exhibit spectral changes due to the SPhP interference. The phase is indeterminate in the spectral regions depicted by horizontal black lines in (c) and the gray areas in (g) because the scattering amplitude from STO is negligibly small in these spectral regions.

polaritons is distinct from the similar case where a standing wave is measured between tip launched and edge reflected surface plasmon-polariton fringes seen in reports on graphene [81] and hexagonal boron nitride [63]. In our work, the radially decaying tip launched SPhPs are weaker than the SPhPs launched from the straight Au edge [61]. It is worth noting that we were able to extract two accurate SPhP dispersions simultaneously over a broad spectral range compared to similar studies on SiC, thus proving the utility of the LSPLS and the potential of STO for far-infrared photonic applications.

The propagation length of the SPhPs, $L_p$, is related to the imaginary part of the SPhP wave vector by $L_p =$

$1/\text{Im}(k_{p,x})$. A comparison of the propagation lengths from our $k_{p,x}$ extracted from the fringe spacings and the propagation lengths calculated from generic theory [Eq. (1)] is shown in the inset of Fig. 4(e). The propagation length of SPhP in the far-IR reststrahlen band is longer than that of the SPhP in the mid-IR reststrahlen band. This is likely due to the relatively lower damping (and lower $\varepsilon_2$) in the far-IR reststrahlen band [see Fig. 1(b) inset]. Interestingly, the high-frequency side of each SPhP shows good agreement with generic theory [Eq. (1)] while the low-frequency side of each SPhP does not. We attribute this disagreement between experiment and generic SPhP theory [Eq. (1)] on the low-frequency side of the
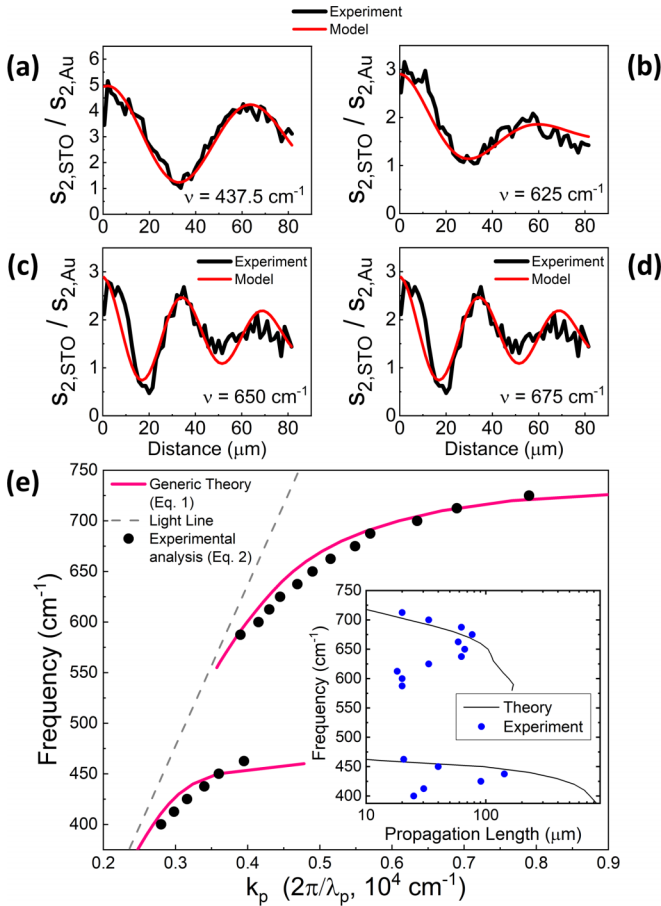
FIG. 4. (a)–(d) Experimental near-field infrared amplitude line cuts from Fig. 3(b) showing fringe spacings at select frequencies. Also shown are fits based on Eq. (2). (e) SPhP dispersion obtained from analysis of experimental results [Eq. (2)] compared to the SPhP dispersion from generic theory [Eq. (1)]. Also included is the light line in vacuum. [(e) inset] Propagation length of SPhPs calculated from generic theory [Eq. (1)] compared to the analysis of experimental results [Eq. (2)].

SPhPs to additional damping introduced by the coupling of the SPhPs to the surface plasmon-polaritons along the shaft of the AFM tip. Our previous work demonstrates that the far-field scattering from the tip is off resonance at frequencies about $400$ cm$^{-1}$ and about $650$ cm$^{-1}$ [21]. These are the frequencies near which the SPhP damping deviates from generic theory [Eq. (1)] prediction. At the tip's off-resonance frequencies, the coupling of the propagating SPhP modes to the tip shaft could be damped.

## IV. CONCLUSIONS AND OUTLOOK

To conclude, we have mapped interference patterns of propagating SPhPs on the surface of single crystal STO in the far- and midinfrared spectral range. This is enabled by a tabletop thermal broadband source based on a laser sustained plasma that provides sufficient intensity in the far- and midinfrared for ultrabroadband sSNOM. We have demonstrated mid- and far-infrared hyperspectral imaging of SPhPs with nanometer scale spatial resolution. This work further makes

the case for STO as a platform for far-infrared nanophotonics. Interesting paths forward include spatially confining these SPhPs to thin films or ultrathin membranes [82,83] of STO as well as incorporating subwavelength nanophotonic structures on STO that guide and direct these SPhPs at wavelengths across the lower reststrahlen band to explore STO's uniquely broad spectral range supporting SPhPs in the terahertz range. It has been shown that STO can be strained to be ferroelectric at room temperature in both thin films and membranes [25,84]. The ferroelectric distortion can be probed by observing a shift in the SPhP resonance wavelength [23,85]. It would be interesting to probe how the SPhP propagation is affected by ferroelectric domains and at domain walls in strained STO films and membranes. The laser sustained plasma light source enables a tabletop method for far-infrared ultrabroadband nanospectroscopy. There is potential for future improvements involving alternative detectors with lower-frequency cutoffs to delve deeper into the far-infrared and terahertz range because the chemical vapor deposition (CVD) diamond window of our infrared light source is transparent to all of the far-infrared and terahertz frequencies.

## ACKNOWLEDGMENTS

## APPENDIX: LASER SUSTAINED PLASMA LIGHT SOURCE

Similar to the Argon Plasma Light Source (APLS), the Laser Sustained Plasma Light Source (LSPLS) comprises an aluminum vessel with windows for optical access and tungsten electrodes for igniting the plasma [20]. For the LSPLS, this vessel is pressurized between 15 and 20 atm gauge of high-purity xenon gas. A high-voltage pulse generates an arc across two electrodes which is then sustained by a constant current. The upgrade consists of a near-infrared diode laser with $\approx 1$ $\mu$m wavelength in the vicinity of a strong xenon line, and incident power of $\approx 85$ W. The laser light is brought to a focus in the gap between these electrodes where the plasma is being sustained by the electric current. The current is then terminated, and the plasma is sustained by the laser at its focus yielding a highly stable and brilliant broadband infrared source. The aluminum vessel has two antireflective coated quartz windows: One window allows us to couple the incident laser to sustain the plasma, and the other window allows the unabsorbed laser light to exit and be terminated at an external beam dump after passing through a beam splitter that sends a small portion of the intensity to a power meter to measure the laser power transmitted through the plasma. A CVD diamond window is clamped to the pressure vessel via a Viton O-ring. The diamond window allows access to the broadband infrared radiation of the plasma into the mid- and far-infrared spectral range while providing the necessary thermal and mechanical properties necessary to seal the pressure vessel. There are major advantages of incorporating the laser to sustain the plasma. In the current sustained plasma in the APLS, a significant
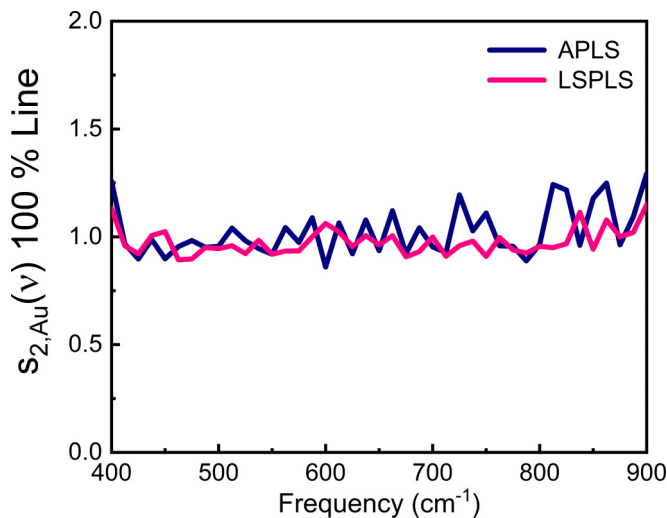
FIG. 5. A 100% line taken on gold (Au) using the APLS [21] and a 100% line taken on gold with the LSPLS in less than half the integration time compared to the APLS (see text for details).

portion of the power is dissipated by the heat conducted by the electrodes. The advantage of sustaining the plasma with a laser is that the power is more efficiently transferred to usable broadband radiation while increasing the lifetime of the light source by significantly lowering the overall usage time of the electrodes. Secondly, the plasma becomes more localized to the focus of the laser, allowing a smaller emission volume which is advantageous for microscopy.

To compare the SNR of our LSPLS with the previous APLS from Refs. [20,21], we show 100% lines taken over gold using the same tip and detector (Fig. 5). A 100% line is the ratio of two spectra obtained one after the other under identical conditions. We note that the integration time for acquisition of spectra with the LSPLS is less than half the integration time for acquisition of spectra with the APLS. Spectra were demodulated at the second harmonic of the tip oscillation frequency. Spectra were obtained with spectral resolution of $\delta\nu = 12.5$ cm$^{-1}$. Gold spectra obtained with the APLS employed an integration time of 120 min per spectrum. Gold spectra obtained with the LSPLS employed an integration time of 55 min per spectrum. The long integration times are required due to the lower detectivity of our wideband MCT detector with low-frequency cutoff of 400 cm$^{-1}$ compared to the commonly used midinfrared MCT detectors such as the high-detectivity Kolmar (KLD-0.1J1/208) that has a low-frequency cutoff of 750 cm$^{-1}$. Using the normalized signal to noise ratio, NSNR $= \frac{\text{SNR}}{\delta\nu\sqrt{t}}$, defined in Ref. [74], we can compare the signal of our LSPLS with the previous APLS. For the demodulated second harmonic ($n = 2$) spectra in the range of 400–850 cm$^{-1}$, we obtain an NSNR of 0.009 $\sqrt{\text{Hz}}$/cm$^{-1}$ and 0.026 $\sqrt{\text{Hz}}$/cm$^{-1}$ for the APLS and the LSPLS, respectively. This result shows that we see almost a threefold increase in our NSNR with the LSPLS system. This leads to lower integration times (of the order of minutes) for obtaining a spectrum, especially on samples with SPhP resonances. For example, it took about 4 min to acquire each spectrum in the hyperspectral line scan on STO [Figs. 3(b) and 3(c)].

[1] C. H. Henry and J. J. Hopfield, Raman Scattering by Polaritons, Phys. Rev. Lett. **15**, 964 (1965).

[2] D. L. Mills and E. Burstein, Polaritons: The electromagnetic modes of media, Reports Prog. Phys. **37**, 817 (1974).

[3] A. V. Zayats, I. I. Smolyaninov, and A. A. Maradudin, Nano-optics of surface plasmon polaritons, Phys. Rep. **408**, 131 (2005).

[4] H. Deng, H. Haug, and Y. Yamamoto, Exciton-polariton Bose-Einstein condensation, Rev. Mod. Phys. **82**, 1489 (2010).

[5] J. Kasprzak, M. Richard, S. Kundermann, A. Baas, P. Jeambrun, J. M. J. Keeling, F. M. Marchetti, M. H. Szymanska, R. Andre, J. L. Staehli, V. Savona, and P. B. Littlewood, Bose-Einstein condensation of exciton polaritons, Nature (London) **443**, 409 (2006).

[6] A. Amo, J. Lefrère, S. Pigeon, C. Adrados, C. Ciuti, I. Carusotto, R. Houdre, E. Giacobino, and A. Bramati, Superfluidity of polaritons in semiconductor microcavities, Nat. Phys. **5**, 805 (2009).

[7] K. G. Lagoudakis, M. Wouters, M. Richard, A. Baas, I. Carusotto, R. Andre, L. S. Dang, and B. Deveaud-Pledran, Quantized vortices in an exciton-polariton condensate, Nat. Phys. **4**, 706 (2008).

[8] S. Kéna-Cohen and S. R. Forrest, Room-temperature polariton lasing in an organic single-crystal microcavity, Nat. Photonics **4**, 371 (2010).

[9] S. Christopoulos, G. B. H. Von Högersthal, A. J. D. Grundy, P. G. Lagoudakis, A. V. Kavokin, J. J. Baumberg, G. Christmann, R. Butté, E. Feltin, J.-F. Carlin, and N. Grandjean, Room-Temperature Polariton Lasing in Semiconductor Microcavities, Phys. Rev. Lett. **98**, 126405 (2007).

[10] D. Ballarini, M. De Giorgi, E. Cancellieri, R. Houdre, E. Giacobino, R. Cingolani, A. Bramati, G. Gigli, and D. Sanvitto, All-optical polariton transistor, Nat. Commun. **4**, 1778 (2013).

[11] X. Zhong, T. Chervy, S. Wang, J. George, A. Thomas, J. A. Hutchinson, E. Devaux, C. Genet, and T. W. Ebbensen, Non-radiative energy transfer mediated by hybrid light-matter states, Angew. Chem., Int. Ed. **55**, 6202 (2016).

[12] J. J. Greffet, R. Carminati, K. Joulain, J. P. Mulet, S. Mainguy, and Y. Chen, Coherent emission of light by thermal sources, Nature (London) **416**, 61 (2002).

[13] R. Hillenbrand, T. Taubner, and F. Keilmann, Phonon-enhanced light–matter interaction at the nanometre scale, Nature (London) **418**, 159 (2002).

[14] N. Ocelic and R. Hillenbrand, Subwavelength-scale tailoring of surface phonon polaritons by focused ion-beam implantation, Nat. Mater. **3**, 606 (2004).

[15] J. D. Caldwell, O. J. Glembocki, Y. Francescato, N. Sharac, V. Giannini, F. J. Bezares, J. P. Long, J. C. Owrutsky, I. Vurgaftman, J. G. Tischler, V. D. Wheeler, and N. D. Bassim, Low-loss, extreme subdiffraction photon confinement via

silicon carbide localized surface phonon polariton resonators, Nano Lett. **13**, 3690 (2013).

[16] G. Shvets, Photonic approach to making a material with a negative index of refraction, Phys. Rev. B **67**, 035109 (2003).

[17] H. S. Kim, N. Y. Ha, J. Y. Park, S. Lee, D. S. Kim, and Y. H. Ahn, Phonon-polaritons in lead halide perovskite film hybridized with THz metamaterials, Nano Lett. **20**, 6690 (2020).

[18] T. Tanabe, K. Suto, J. Nishizawa, K. Saito, and T. Kimura, Frequency-tunable terahertz wave generation via excitation of phonon-polaritons in GaP, J. Phys. D: Appl. Phys. **36**, 953 (2003).

[19] K. Ohtani, B. Meng, M. Franckié, L. Bosco, C. Ndebeka-Bandou, M. Beck, and J. Faist, An electrically pumped phonon-polariton laser, Sci. Adv. **5**, eaau1632 (2019).

[20] D. J. Lahneman, T. J. Huffman, P. Xu, S. L. Wang, T. Grogan, and M. M. Qazilbash, Broadband near-field infrared spectroscopy with a high temperature plasma light source, Opt. Express **25**, 20421 (2017).

[21] P. McArdle, D. J. Lahneman, A. Biswas, F. Keilmann, and M. M. Qazilbash, Near-field infrared nanospectroscopy of surface phonon-polariton resonances, Phys. Rev. Research **2**, 023272 (2020).

[22] M. Lewin, C. Baeumer, F. Gunkel, A. Schwedt, F. Gaussmann, J. Wueppen, J. Meuffels, B. Jungbluth, J. Mayer, R. Dittmann, R. Waser, and T. Taubner, Nanospectroscopy of infrared phonon resonance enables local quantification of electronic properties in doped SrTiO$_3$ ceramics, Adv. Funct. Mater. **28**, 1802834 (2018).

[23] L. Wehmeier, D. Lang, Y. Liu, X. Zhang, S. Winnerl, L. M. Eng, and S. C. Kehr, Polarization-dependent near-field phonon nanoscopy of oxides: SrTiO$_3$, LiNbO$_3$, and PbZr$_{0.2}$Ti$_{0.8}$O$_3$, Phys. Rev. B **100**, 035444 (2019).

[24] A. A. Sirenko, A. M. Clark, J. Hao, W. Si, and X. X. Xi, Soft-mode hardening in SrTiO$_3$ thin films, Nature (London) **404**, 373 (2000).

[25] J. H. Haeni, P. Irvin, W. Chang, R. Uecker, P. Reiche, Y. L. Li, S. Choudhury, W. Tian, M. E. Hawley, B. Craigo, A. K. Tagantsev, and X. Q. Pan, Room-temperature ferroelectricity in strained SrTiO$_3$, Nature (London) **430**, 758 (2004).

[26] S. Zollner, A. A. Demkov, R. Liu, P. L. Fejes, R. B. Gregory, P. Alluri, J. A. Curless, Z. Yu, J. Ramdani, R. Droopad, T. E. Tiwald, and J. N. Hilfiker, Optical properties of bulk and thin-film SrTiO$_3$ on Si and Pt, J. Vac. Sci. Technol. B: Microelectron. Nanometer Struct. Process. Meas. Phenom. **18**, 2242 (2000).

[27] A. Sendil Kumar, P. Suresh, M. Mahesh Kumar, H. Srikanth, M. L. Post, K. Sahner, R. Moos, and S. Srinath, Magnetic and ferroelectric properties of Fe doped SrTiO$_{3-\delta}$ films, J. Phys.: Conf. Ser. **200**, 092010 (2010).

[28] S. Taibl, G. Fafilek, and J. Fleig, Impedance spectra of Fe-doped SrTiO$_3$ thin films upon bias voltage: Inductive loops as a trace of ion motion, Nanoscale **8**, 13954 (2016).

[29] O. N. Tufte and P. W. Chapman, Electron mobility in semiconducting strontium titanate, Phys. Rev. **155**, 796 (1967).

[30] J. L. M. Van Mechelen, D. Van Der Marel, C. Grimaldi, A. B. Kuzmenko, N. P. Armitage, N. Reyren, H. Hagemann, and I. I. Mazin, Electron-Phonon Interaction and Charge Carrier Mass Enhancement in SrTiO$_3$, Phys. Rev. Lett. **100**, 226403 (2008).

[31] W. Baer, Free-carrier absorption in reduced SrTiO$_3$, Phys. Rev. **144**, 734 (1966).

[32] I. H. Kwak, S. S. Varnoosfaderani, C. S. Barquist, A. Paykar, A. Shakya, Y. Lee, A. F. Hebard, and A. Biswas, Optimization of atomically smooth and metallic surface of SrTiO$_3$, J. Appl. Phys. **121**, 135305 (2017).

[33] P. P. Balakrishnan, M. J. Veit, U. S. Alaan, M. T. Gray, and Y. Suzuki, Metallicity in SrTiO$_3$ substrates induced by pulsed laser deposition, APL Mater. **7**, 011102 (2019).

[34] X. Lin, C. W. Rischau, L. Buchauer, A. Jaoui, B. Fauqué, and K. Behnia, Metallicity without quasi-particles in room-temperature strontium titanate, npj Quantum Mater. **2**, 41 (2017).

[35] A. Ohtomo and H. Y. Hwang, A high-mobility electron gas at the LaAlO$_3$/SrTiO$_3$ heterointerface, Nature (London) **427**, 423 (2004).

[36] A. F. Santander-Syro, O. Copie, T. Kondo, F. Fortuna, S. Pailhes, R. Weht, X. G. Qiu, F. Bertran, A. Nicolaou, A. Taleb-Ibrahimi, P. Le Fvre, and G. Herranz, Two-dimensional electron gas with universal subbands at the surface of SrTiO$_3$, Nature (London) **469**, 189 (2011).

[37] J. F. Schooley, W. R. Hosler, and M. L. Cohen, Superconductivity in Semiconducting SrTiO$_3$, Phys. Rev. Lett. **12**, 474 (1964).

[38] G. Binnig, A. Baratoff, H. E. Hoenig, and J. G. Bednorz, Two-Band Superconductivity in Nb-Doped SrTiO$_3$, Phys. Rev. Lett. **45**, 1352 (1980).

[39] D. P. Norton, Synthesis and properties of epitaxial electronic oxide thin-film materials, Mater. Sci. Eng., R **43**, 139 (2004).

[40] N. Kalfagiannis, J. L. Stoner, J. Hillier, I. Vangelidis, and E. Lidorikis, Mid- to far-infrared sensing: SrTiO$_3$, a novel optical material, J. Mater. Chem. C **7**, 7851 (2019).

[41] Y. Zhong, S. D. Malagari, T. Hamilton, and D. Wasserman, Review of mid-infrared plasmonic materials, J. Nanophotonics **9**, 093791 (2015).

[42] J. D. Caldwell, L. Lindsay, V. Giannini, I. Vurgaftman, T. L. Reinecke, S. A. Maier, and O. J. Glembocki, Low-loss, infrared and terahertz nanophotonics using surface phonon polaritons, Nanophotonics **4**, 44 (2015).

[43] R. A. Cowley, Lattice dynamics and phase transitions of strontium titanate, Phys. Rev. **134**, A981 (1964).

[44] G. Álvarez-Pérez, T. G. Folland, I. Errea, J. Taboada-Gutiérrez, J. Duan, J. Martín-Sánchez, A. I. F. Tresguerres-Mata, J. R. Matson, A. Bylinkin, M. He, W. Ma, Q. Bao, J. I. Martín, J. D. Caldwell, A. Y. Nikitin, and P. Alonso-González, Infrared permittivity of the biaxial van der Waals semiconductor α-MoO$_3$ from near- and far-field correlative studies, Adv. Mat. **32**, 1908176 (2020).

[45] T. Azuhata and K. Shimada, Polar phonons in β-Ga$_2$O$_3$ studied by IR reflectance spectroscopy and first-principle calculations, Appl. Phys. Express **10**, 081101 (2017).

[46] P. Dore, G. De Marzi, and A. Paolone, Refractive indices of SrTiO$_3$ in the infrared region, Int. J. Infrared Millimeter Waves **18**, 125 (1997).

[47] T. G. Folland, L. Nordin, D. Wasserman, and J. D. Caldwell, Probing polaritons in the mid- to far-infrared, J. Appl. Phys. **125**, 191102 (2019).

[48] F. Keilmann and R. Hillenbrand, Near-field microscopy by elastic light scattering from a tip, Philos. Trans. R. Soc. A **362**, 787 (2004).

[49] M. M. Qazilbash, M. Brehm, B.-G. Chae, P.-C. Ho, G. O. Andreev, B.-J. Kim, S. J. Yun, A. V. Balatsky, M. B. Maple, F. Keilmann, H.-T. Kim, and D. N. Basov, Mott transition in VO$_2$

revealed by infrared spectroscopy and nano-imaging, Science **318**, 1750 (2007).

[50] F. Huth, A. Govyadinov, S. Amarie, W. Nuansing, F. Keilmann, and R. Hillenbrand, Nano-FTIR absorption spectroscopy of molecular fingerprints at 20 nm spatial resolution, Nano Lett. **12**, 3973 (2012).

[51] X. Lu, O. Khatib, X. Du, J. Duan, W. Wei, X. Liu, H. A. Bechtel, F. D'Apuzzo, M. Yan, A. Buyanin, Q. Fu, J. Chen, M. Salmeron, J. Zeng, M. B. Raschke, P. Jiang, and X. Bao, Nanoimaging of electronic heterogeneity in $Bi_2Se_3$ and $Sb_2Te_3$ nanocrystals, Adv. Electron. Mater. **4**, 1700377 (2018).

[52] M. B. Raschke and C. Lienau, Apertureless near-field optical microscopy: Tip-sample coupling in elastic light scattering, Appl. Phys. Lett. **83**, 5089 (2003).

[53] J. M. Atkin, S. Berweger, A. C. Jones, and M. B. Raschke, Nano-optical imaging and spectroscopy of order, phases, and domains in complex solids, Adv. Phys. **61**, 745 (2012).

[54] J. Renger, S. Grafström, L. M. Eng, and R. Hillenbrand, Resonant light scattering by near-field-induced phonon polaritons, Phys. Rev. B **71**, 075410 (2005).

[55] A. Huber, N. Ocelic, D. Kazantsev, and R. Hillenbrand, Near-field imaging of mid-infrared surface phonon polariton propagation, Appl. Phys. Lett. **87**, 081103 (2005).

[56] P. Hermann, A. Hoehl, G. Ulrich, C. Fleischmann, A. Hermenlink, B. Kastner, P. Patoka, A. Hornemann, B. Backhoff, E. Ruhl, and G. Ulm, Characterization of semiconductor materials using synchrotron radiation-based near-field infrared microscopy and nano-FTIR spectroscopy, Opt. Express **22**, 17948 (2014).

[57] S. Amarie, T. Ganz, and F. Keilmann, mid-infrared near-field spectroscopy, Opt. Express **17**, 21794 (2009).

[58] S. Amarie and F. Keilmann, Broadband-infrared assessment of phonon resonance in scattering-type near-field microscopy, Phys. Rev. B **83**, 045404 (2011).

[59] A. Huber, N. Ocelic, T. Taubner, and R. Hillenbrand, Nanoscale resolved infrared probing of crystal structure and of plasmon-phonon coupling, Nano Lett. **6**, 774 (2006).

[60] V. E. Babicheva, S. Gamage, L. Zhen, S. B. Cronin, V. S. Yakovlev, and Y. Abate, Near-field surface waves in few-layer $MoS_2$, ACS Photonics **5**, 2106 (2018).

[61] S. Dai, Q. Ma, Y. Yang, J. Rosenfeld, M. D. Goldflam, A. McLeod, Z. Sun, T. I. Andersen, Z. Fei, M. Liu, Y. Shao, K. Watanabe, T. Taniguchi, M. Thiemens, F. Keilmann, P. Jarillo-Herrero, M. M. Fogler, and D. N. Basov, Efficiency of launching highly confined polaritons by infrared light incident on a hyperbolic material, Nano Lett. **17**, 5285 (2017).

[62] S. Dai, Q. Ma, M. K. Liu, T. Andersen, Z. Fei, M. D. Goldflam, M. Wagner, K. Watanabe, T. Taniguchi, M. Thiemens, F. Keilmann, G. C. A. M. Janssen, S.-E. Zhu, P. Jarillo-Herrero, M. M. Fogler, and D. N. Basov, Graphene on hexagonal boron nitride as a tunable hyperbolic metamaterial, Nat. Nanotechnol. **10**, 682 (2015).

[63] Z. Shi, H. A. Bechtel, S. Berweger, Y. Sun, B. Zeng, C. Jin, H. Chang, M. C. Martin, M. B. Raschke, and F. Wang, Amplitude- and phase-resolved nanospectral imaging of phonon polaritons in hexagonal boron nitride, ACS Photonics **2**, 790 (2015).

[64] S. Dai, Z. Fei, Q. Ma, A. S. Rodin, M. Wagner, A. S. McLeod, M. K. Liu, W. Gannett, W. Regan, K. Watanabe, T. Taniguchi, M. Thiemens, G. Dominguez, A. H. Castro Neto, A. Zettl, F. Keilmann, P. Jarillo-Herrero, M. M. Fogler, and D. N. Basov,

Tunable phonon polaritons in atomically thin van der Waals crystals of boron nitride, Science **343**, 1125 (2014).

[65] I. D. Barcelos, T. A. Canassa, R. A. Mayer, F. H. Feres, E. G. de Oliveira, A. B. Goncalves, H. A. Bechtel, R. O. Freitas, F. C. B. Maia, and D. C. B. Alves, Ultrabroadband nanocavity of hyperbolic phonon−polaritons in 1D-like $\alpha$-$MoO_3$, ACS Photonics **8**, 3026 (2021).

[66] F. H. Feres, R. A. Mayer, L. Wehmeier, F. C. B. Maia, E. R. Viana, A. Malachias, H. A. Bechtel, J. M. Klopf, L. M. Eng, S. C. Kehr, J. C. González, R. O. Freitas, and I. D. Barcelos, Sub-diffractional cavity modes of terahertz hyperbolic phonon polaritons in tin oxide, Nat. Commun. **12**, 1995 (2021).

[67] Z. Yao, X. Chen, L. Wehmeier, S. Xu, Y. Shao, Z. Zeng, F. Liu, A. S. Mcleod, S. N. Gilbert Corder, M. Tsuneto, W. Shi, Z. Wang, W. Zheng, H. A. Bechtel, G. L. Carr, M. C. Martin, A. Zettl, D. N. Basov, X. Chen, L. M. Eng *et al.*, Probing subwavelength in-plane anisotropy with antenna-assisted infrared nano-spectroscopy, Nat. Commun. **12**, 2649 (2021).

[68] S. N. Neal, H.-S. Kim, K. A. Smith, A. V. Haglund, D. G. Mandrus, H. A. Bechtel, G. L. Carr, K. Haule, D. Vanderbilt, and J. L. Musfeldt, Near-field infrared spectroscopy of monolayer $MnPS_3$, Phys. Rev. B. **100**, 075428 (2019).

[69] O. Khatib, H. A. Bechtel, M. C. Martin, M. B. Raschke, and G. L. Carr, Far Infrared synchrotron near-field nanoimaging and nanospectroscopy, ACS Photonics **5**, 2773 (2018).

[70] M. M. Qazilbash and D. J. Lahneman, Infrared light generating system, U.S. Patent No. 9,934,927 B1 (April 3, 2018).

[71] A. Gozar, N. E. Litombe, J. E. Hoffman, and I. Božovic, Optical nanoscopy of high-$T_c$ cuprate nano-constriction devices patterned by helium ion beams, Nano Lett. **17**, 1582 (2017).

[72] B. Hauer, A. P. Engelhardt, and T. Taubner, Quasi-analytical model for scattering infrared near-field microscopy on layered systems, Opt. Express **20**, 13173 (2012).

[73] R. Krutokhvostov, A. A. Govyadinov, J. M. Stiegler, F. Huth, A. Chuvilin, P. S. Carney, and R. Hillenbrand, Enhanced resolution in subsurface near-field optical microscopy, Opt. Express **20**, 593 (2012).

[74] B. T. O'Callahan, W. E. Lewis, S. Möbius, J. C. Stanley, E. A. Muller, and M. B. Raschke, Broadband infrared vibrational nano-spectroscopy using thermal blackbody radiation, Opt. Express **23**, 32063 (2015).

[75] F. Huth, M. Schnell, J. Wittborn, N. Ocelic, and R. Hillenbrand, Infrared-spectroscopic nanoimaging with a thermal source, Nat. Mater. **10**, 352 (2011).

[76] T. Dougakiuchi, Y. Kawada, and G. Takebe, Continuous multispectral imaging of surface phonon polaritons on silicon carbide with an external cavity quantum cascade laser, Appl. Phys. Express **11**, 032001 (2018).

[77] A. Y. Nikitin, E. Yoxall, M. Schnell, S. Velez, I. Dolado, P. Alonso-Gonzalez, F. Casanova, L. E. Hueso, and R. Hillenbrand, Nanofocusing of hyperbolic phonon polaritons in a tapered boron nitride slab, ACS Photonics **3**, 924 (2016).

[78] A. Woessner, Y. Gao, I. Torre, M. B. Lundeberg, C. Tan, K. Watanabe, T. Taniguchi, R. Hillenbrand, J. Hone, M. Polini, and F. H. L. Koppens, Electrical $2\pi$ phase control of infrared light in a 350-nm footprint using graphene plasmons, Nat. Photonics **11**, 421 (2017).

[79] Y. Li, N. Zhou, E. C. Kinzel, X. Ren, and X. Xu, The origin of interferometric effect involving surface plasmon polariton in

scattering near-field scanning optical microscopy, Opt. Express **22**, 2965 (2014).

[80] R. Hillenbrand and F. Keilmann, Complex Optical Constants on a Subwavelength Scale, Phys. Rev. Lett. **85**, 3029 (2000).

[81] Z. Fei, A. S. Rodin, G. O. Andreev, W. Bao, A. S. McLeod, M. Wagner, L. M. Zhang, Z. Zhao, M. Thiemens, G. Dominguez, M. M. Fogler, A. H. Castro-Neto, C. N. Lau, F. Keilmann, and D. N. Basov, Gate-tuning of graphene plasmons revealed by infrared nano-imaging, Nature (London) **487**, 82 (2012).

[82] S. S. Hong, J. H. Yu, D. Lu, A. F. Marshall, Y. Hikita, Y. Cui, and H. Y. Hwang, Two-dimensional limit of crystalline order in perovskite membrane films, Sci. Adv. **3**, eaao5173 (2017).

[83] D. M. Juraschek and P. Narang, Highly confined phonon polaritons in monolayers of perovskite oxides, Nano Lett. **21**, 5098 (2021).

[84] R. Xu, J. Huang, E. S. Barnard, S. S. Hong, P. Singh, E. K. Wong, T. Jansen, V. Harbola, J. Xiao, B. Y. Wang, S. Crossley, D. Lu, S. Liu, and H. Y. Hwang, Strain-induced room-temperature ferroelectricity in $SrTiO_3$ membranes, Nat. Commun. **11**, 3141 (2020).

[85] J. Döring, D. Lang, L. Wehmeier, F. Kuschewski, T. Nörenberg, S. C. Kehr, and L. M. Eng, Low-temperature nanospectroscopy of the structural ferroelectric phases in single-crystalline barium titanate, Nanoscale **10**, 18074 (2018).